

Beyond Exascale: Dataflow Domain Translation on a Cerebras Cluster

TOMAS OPPELSTRUP, Cerebras Systems, USA

NICHOLAS GIAMBLANCO, Cerebras Systems, Canada

DELYAN Z. KALCHEV, Cerebras Systems, USA

ILYA SHARAPOV, Cerebras Systems, USA

MARK TAYLOR, Sandia National Laboratories, USA

DIRK VAN ESSENDELFT, National Energy Technology Laboratory, USA

SIVASANKARAN RAJAMANICKAM, Sandia National Laboratories, USA

MICHAEL JAMES, Cerebras Systems, USA

Simulation of physical systems is essential in many scientific and engineering domains. Commonly used domain decomposition methods are unable to deliver high simulation rate or high utilization in network computing environments. In particular, Exascale systems deliver only a small fraction their peak performance for these workloads. This paper introduces the novel Domain Translation algorithm, designed to overcome these limitations. We apply this method and show simulations running in excess of 1.6 million time steps per second and simulations achieving 84 PFLOP/s. Our implementation can achieve 90% of peak performance in both single-node and clustered environments. We illustrate the method by applying the shallow-water equations to model a tsunami following an asteroid impact at 460m-resolution on a planetary scale running on a cluster of 64 Cerebras CS-3 systems.

Additional Key Words and Phrases: Cluster Computing, Time Integration, Stencil Computations, Finite Difference Methods, Shallow Water Equations

ACM Reference Format:

Tomas Oppelstrup, Nicholas Giamblanco, Delyan Z. Kalchev, Ilya Sharapov, Mark Taylor, Dirk Van Essendelft, Sivasankaran Rajamanickam, and Michael James. 2025. Beyond Exascale: Dataflow Domain Translation on a Cerebras Cluster. In *Proceedings of HPC Asia*. ACM, New York, NY, USA, 19 pages. <https://doi.org/tbd>

1 Introduction

The “principle of locality” in physics asserts that objects are influenced only by their immediate surroundings. This principle applies to both space and time. It also forms the basis for Partial Differential Equations (PDEs) that relate rate of change at a point in space to local gradients. PDEs describe various physical phenomena, including waves, potentials, diffusion, fluid motion, and electromagnetism. With the development of numerical methods like finite difference, finite

Corresponding authors emails: michael@cerebras.net, srajama@sandia.gov.

Authors’ Contact Information: Tomas Oppelstrup, Cerebras Systems, Sunnyvale, CA, USA; Nicholas Giamblanco, Cerebras Systems, Vancouver, BC, Canada; Delyan Z. Kalchev, Cerebras Systems, Sunnyvale, CA, USA; Ilya Sharapov, Cerebras Systems, Sunnyvale, CA, USA; Mark Taylor, Sandia National Laboratories, Albuquerque, NM, USA; Dirk Van Essendelft, National Energy Technology Laboratory, Morgantown, WV, USA; Sivasankaran Rajamanickam, Sandia National Laboratories, Albuquerque, NM, USA; Michael James, Cerebras Systems, Sunnyvale, CA, USA.

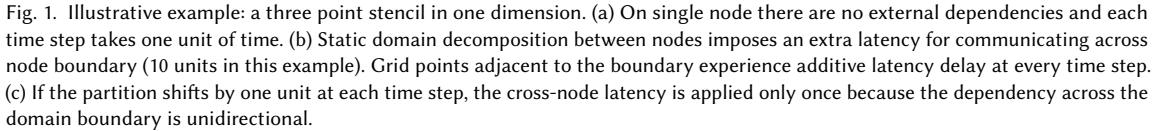
Permission to make digital or hard copies of all or part of this work for personal or classroom use is granted without fee provided that copies are not made or distributed for profit or commercial advantage and that copies bear this notice and the full citation on the first page. Copyrights for components of this work owned by others than the author(s) must be honored. Abstracting with credit is permitted. To copy otherwise, or republish, to post on servers or to redistribute to lists, requires prior specific permission and/or a fee. Request permissions from permissions@acm.org.

© 2025 Copyright held by the owner/author(s). Publication rights licensed to ACM.

Manuscript submitted to ACM

Manuscript submitted to ACM

1



Clusters of Von Neumann computers have been used to simulate ever larger systems. This has culminated in the Exascale Computing Project which ended in 2024 [2, 17]. While the physical dimensions or resolution of the systems we could study grew by weak scaling, the temporal evolution rate has largely stalled due to the failure of strong scaling on Von Neumann architectures (i.e., the memory wall). Most typical earth system models achieve less than 5% of peak performance [12]. Even with large peta- and exa-class machines, most large scale models achieve between 1.2 and 8 PFLOP/s, with the largest being 25.96 PFLOP/s [9, 10, 19, 35, 36].

We present the first distributed PDE solver on a cluster of WSEs. Further, we introduce a novel approach, based on the principle of locality, that maintains both physical and temporal locality across this spatial architecture so that networking latencies are completely hidden. We demonstrate the method by applying it to the solve two systems: (1) the heat equation (HE) and (2) full-Earth tsunami simulations using Shallow Water Equations (SWE).

Manuscript submitted to ACM

Although this method is data-intensive, our demonstration runs achieve over 60% computational peak utilization on a large cluster. As we will demonstrate, this approach, in combination with the spatial architecture, is able to achieve perfect weak scaling at all tested processor workloads and maintain high efficiency down to just 256 elements per processor. The achieved 84 PFLOP/s (66% of system peak) is unprecedented for stencil computations.

The rest of the paper is organized as follows. The next section introduces Domain Translation, the new latency-hiding algorithm, discusses its properties, and compares it to traditional methods. Section 3 describes the implementation of the method on a cluster of Cerebras WSE systems. Section 4 characterizes the performance of the method applied to the heat and shallow water equations. Finally, the conclusion summarizes the results and describes how they advance the state of the art.

2 Domain Translation Method

2.1 Distributed computations with domain decomposition

Cluster implementations of geometry-based simulations typically use the domain decomposition method with different parts of the discretized mesh mapped to different nodes. These simulations, including stencil computations, tend to have low operational intensity [33], which makes it challenging to minimize the effects of communication in distributed implementations. Special cases, such as Krylov solvers, can benefit from communication avoiding techniques [5]. These specialized techniques use redundant computation to minimize data exchange between communicating nodes [14].

| Symbol | Unit | Description |
|-----------|-------|---|
| τ | s | Latency - Time of flight on network link |
| n | pts | Grid points - Linear span of grid points |
| g | pts | Ghost width - Thickness of overlap region |
| p | pts | Stencil reach - Manhattan stencil radius |
| t | s | Iteration time - Computing full time step |
| f | Hz | Iteration frequency - Rate of time stepping |
| c | s | Serial time - Computing one grid point |
| d | | Dimension - Dimensionality of domain |
| w | cores | Fabric Size - Linear span of core array |
| ϕ | | Latitude |
| λ | | Longitude |
| ℓ | | Coriolis force |

Table 1. Notation and variables

A stencil computation’s asymptotic iteration rate can not exceed the rate of the slowest grid point. For a stencil with range p , grid points exchange data within a p -neighborhood. In a direct fixed mapping for domain decomposition methods [27], this exchange causes grid points adjacent to a subdomain boundary to incur network latency on every step. Thus, rate-limiting the entire simulation based on the slowest network link with latency τ to $1/\tau$ (Figure 1b).

For distributed stencil computations, a common approach is to replicate a layer of *ghost* points [6] to adjacent nodes [16]. Each node holds replicated ghost values that belong to its neighbors’ subdomains. These ghost values participate in the computation, but after each iteration the ghost values at the outermost extent have undefined values because they do not have access to information from the neighboring node. For the ghost method to reach a target iteration rate f in the presence of network latency, the ghost region’s thickness g must be proportional to τf . When n is the largest

| Method | Utilization Multiplier | Frequency Limit | Utilization at Max Speed |
|----------------------------------|------------------------|-----------------|--------------------------|
| Static Domain Decomposition | 1 | latency | $c/\tau \ll 1$ |
| Overlapping Domain Decomposition | $(1 - f\tau/n)^d$ | bandwidth | $1/(f\tau)^d \ll 1$ |
| Domain translation (Our Method) | 1 | bandwidth | 1 |

Table 2. Comparison of domain decomposition methods.

feasible domain radius for a node to achieve f , the volume-fraction of the ghost region for a d -dimensional domain is $1 - \left(\frac{n-2g}{n}\right)^d$. This implies utilization decreases as rapidly as a degree- d polynomial in τf .

While the overlap method amortizes the internode latency over multiple elements, it always sacrifices efficiency as it relies on redundant re-computations. It also forces a trade-off: increasing the rate of time step processing requires increasing the size of the ghost region, reducing both computational and power efficiency.

This work demonstrates PDE solutions running on a large cluster in a compute-bound regime fully independent of inter-node network latency. The achievement is based on a novel algorithm and its implementation on the WSE. Our implementation allows strong-scaling up to 1.5 million timesteps per second across a cluster with $10\mu\text{s}$ interconnect latency.

2.2 Domain Translation algorithm

We introduce *Domain Translation*, a parallel algorithm for computing a stencil code efficiently over high-latency network links. We will develop the algorithm presentation in a one-dimensional setting (Figure 1a). The same principles hold in higher dimensions. The algorithm requires nodes be connected in a ring (torus).

Application of a stencil operator uses information from grid points within a distance $\pm p$. Normally, this means that network links connecting subdomains carry bi-directional network traffic originating from p points on each side of the link.

The domain translation algorithm translates the mapping from grid-points to processors by p grid points on each iteration. From the perspective of a network's links, translation composed with the stencil operator exchange causes unidirectional traffic flow. Grid data now travels $2p$ in the direction of translation and never travels against this direction.

Adjacent nodes have distinct *upstream* and *downstream* relationships. This unidirectional flow avoids additive buildup of latency contributions (Figure 1c). A given grid point only experiences network latency after it has crossed a node's entire subdomain. In this way, the impact of network latency is amortized over the width of the subdomain. In contrast, a fixed partitioning domain decomposition of a fixed subset of gridpoints would experience latency cost every iteration (Figure 1b).

As we will show, network latency causes no utilization loss when the size of a subdomain exceeds a critical threshold. Only link bandwidth and computational performance limit the iteration rate. We note the algorithm requires additional network bandwidth both because it supports higher iteration rates and because local grid-point state that does not participate in stencil state exchange transits network links to stay with its grid point as the domain translates.

Consider each node as a serial processor holding n grid points. Each node can compute $n - 2p$ interior grid points' next state immediately, before any network data arrives (Figure 2). Nodes can do this recursively for $n/(2p)$ steps to complete the space-time triangle with base n and height $n/(2p)$. As each row completes, the node records a *package* of $2p$ grid points' values that will be used by the downstream node. For our analysis, note that these initial downstream packages are available for transmission before a node receives any upstream packages.

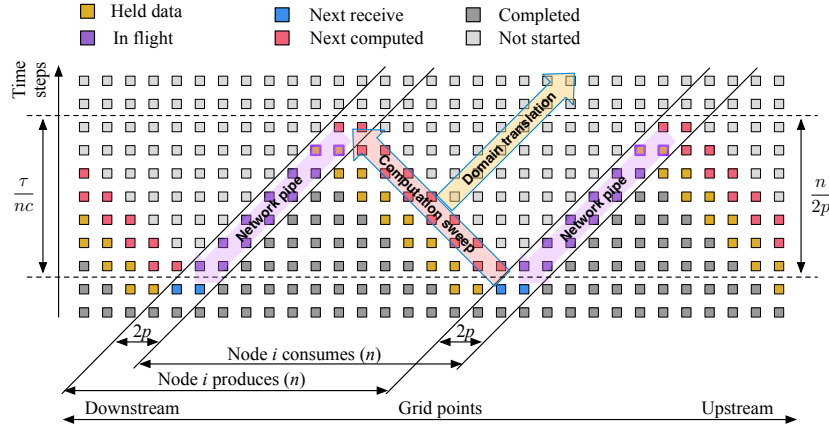


Fig. 2. Domain translation method. Diagram shows grid points (x-axis) by timestep (y-axis). The diagonal lines indicate high-latency subdomain boundaries. The diagram depicts the algorithm's steady-state duty cycle. When the node receives a package (blue) it initiates a computation sweep that uses stored values (yellow) to produce the new grid point state (red). At the end of the sweep it submits its last computed values into the downstream network pipeline. The time used to complete the computation sweep is the same time it takes a network package to advance one "step" through the network pipeline. The end-to-end network latency coincides with $n/2p$ steps. The processor's wall-clock time proceeds in the direction of the "domain translation" arrow. Note that in the processor's time frame, it proceeds through a full network pipeline's worth of computation sweeps prior to receiving data that had just entered the upstream network pipeline.

2.3 Hardware constraints

Compute performance, network latency, and network bandwidth each impose an application-performance limit:

Compute Limit For every package a node receives, it is able to compute the next width- p upstream facing edge of its space-time state chart. As the edge grows the diagram elongates the initial triangle into a parallelogram (Figure 2). Each package provides input needed for n grid-point computation steps. Assuming that it takes c time to process each point update, in the compute-bound scenario the nodes produce and consume packages at a rate of $1/(cn)$.

Latency Limit The network can not sustain a rate greater than the equal spacing of the $n/(2p)$ initially held packages in the network pipeline. Therefore latency-bound links deliver packages at a rate of $n/(2p\lambda)$. Combining the latency-limited and compute-limited expressions, shows full utilization of compute-bound performance when $n^2 > 2p\lambda/c$.

Bandwidth Limit In addition to these constraints of compute throughput and network latency, network bandwidth bounds package transmission rate proportionally to the number of boundary points or n^{d-1} . In the case of $d = 1$, the bandwidth limit is a fixed cap independent of n .

Figure 3 illustrates the combined effect of network and computational constraints. If the number of grid points per node is small, the simulation is network latency dominated. As we increase this number, the constraint shifts to either bandwidth, or computational throughput. In the latter case, both bandwidth and latency of the network are fully hidden, allowing the nodes to run at full kernel efficiency.

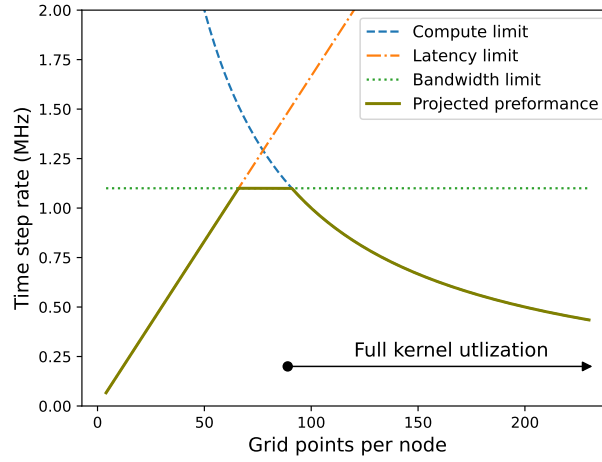


Fig. 3. Time step rate can be limited by the network latency, bandwidth, or compute throughput. If the number of grid points per node is sufficiently large, the network effects are fully hidden and the kernels are expected to run at full computational utilization.

2.4 Dataflow Approach

There is inherent symmetry in the way that this method mimics the principle of locality in physics on computer hardware. Spatial architectures differ from Von Neumann architectures in the topology of the memory/processor system. In Von Neumann architectures, there is a vertical data flow between each processor and its various caches as well as main memory. Transmission between processors is typically done by shared memory access and the wire density limits to main memory create significant access limits. Further being tied to the same memory pool at all times with all processors limits the asynchronous capabilities of the processors. That is, they have to be working on the same time step (or agreed chunk of time) within the same execution pathway.

Spatial architectures offer a compelling alternative to traditional von Neumann-based processors for scientific workloads that exhibit high degrees of data parallelism and spatial locality.

Spatial architectures are different. Main memory is distributed evenly with the processors and is at the nano scale. This allows memory bandwidth to be perfectly matched to processor speed. Processors are directly connected with a Network-on-Chip (NoC) router (also at nano scale) which allows data to be transmitted in parallel with low energy penalty in a very rapid, but reliable transmission. Thus the processor/memory topology is completely flat without memory hierarchy. Computation is explicitly mapped onto an array of processing elements (PEs). The distributed memory model removes synchronization bottlenecks related to memory accesses, which frequently limit performance in conventional HPC systems. By colocating data and computation, spatial architectures enable efficient use of memory bandwidth and energy, particularly for compute and memory intensive kernels commonly found in numerical simulation, finite-element methods, and stencil computations.

The NoC connectivity allows for asynchronous, decentralized execution. Each PE can operate independently, performing computations and exchanging data with a fixed set of neighbors without global synchronization. This neighbor-to-neighbor communication model supports fine-grained parallelism and allows data to stream through the compute fabric while intermediate results are processed in-place. As a result, spatial architectures can sustain high

throughput and deterministic execution patterns—attributes critical for large-scale simulations and time-stepped solvers. Their ability to exploit both spatial and temporal locality makes them well-suited for accelerating structured grid computations and other spatially-amenable problems in scientific computing. As we will show in the next section, these features of spatial architectures allow a very simple and elegant implementation of the Domain Translation algorithm.

To implement Domain Translation, we can take advantage of the spatial hardware architecture by tilting the calculation plane in space-time by 45 degrees (see Figure 2). This is very similar to maintaining the concept of "now" on a Penrose diagram as light moves through space time. On hardware, data is shifted up and to the left in time while the space relative to "now" is always left/right. This ensures that all data movements are at most 2 processor hops away in the case of time evolution and 1 hop in space. In this way, all relevant data lives in the local neighborhood of the processor operating on it at all times, regardless of when "now" is. Said another way, the data and instruction execution pathway are always coincident and local on all processors at every execution cycle at every point in the simulation (regardless of how many wafers are involved). Further, there is no need for host-device interaction; the entire cluster execution is self orchestrated after compile time. Finally, applying similar concepts to relativity in computing allows us to segment "now" across multiple wafers at once such that our time horizon extends past the latency barrier between wafers. As long as the calculation time horizon on each wafer is larger than the network latency, the latency can be completely hidden and allow efficient scaling to large clusters.

3 Implementation on Wafer Scale Engine

This section describes the domain translation software framework that we developed and the hardware used in our experiments.

3.1 Stencil Implementation

We implemented a generic stencil-code framework in the Tungsten dataflow language [24]. The framework allows declaring state variables, defining time-stepping operators, and invoking translation primitives to moves data by a (p, p) -step in the grid space with a combination of memory copy and network transmission.

The framework itself is lean and consists of 1,000 lines of code, including core-to-core and node-to-node communication and all kernel functions.

Each core holds $n \times n$ grid points. At compile time, we specify n ; (w_w, w_h) , the number of cores to use on each node; and q , the amount of node-to-node interconnection bandwidth to allocate. To load the program on a cluster, we provide a graph of nodes (identified by their network addresses) for establishing software-defined network links that connect adjacent subdomains. The graph has annotations with initial condition data for each subdomain.

The framework initiates program execution by setting all nodes to run. This is an inherently an asynchronous process. For consistent performance measurements, we synchronize the wafers and cores before beginning the time stepping loop.

We implemented the Heat Equation using 5-point and 9-point central difference schemes (50 lines of code), and the Shallow Water Equations (700 lines of code) to characterize the performance of the Domain Translation algorithm on the WSE cluster. The listing for the core functions in the 5-point heat equation code is shown in Table 3. The different equations differ in their variable counts and arithmetic intensities. By varying the types of loads we are better able to characterize performance.

```

1  sp socket right,up,down,left; // Communication sockets
2
3  xp param n,p;           // Grid size n x n, and p = stencil width = translation distance
4  xp const w = 2*p;       // Width of communication layer
5  sp x[n+w][n+w];         // Solution
6  sp y[n+w][n+w];         // Temporary to hold next timestep
7  sp avec[5];             // Stencil weights: a(-1,0), a(0,-1), a(1,0), a(0,1), a(0,0)
8                          // a(*,*) set to reflect a 5-point Laplacian in space with
9                          // forward Euler intgeration in time.
10
11 function sendrecv() {
12   parallel {
13     Vi ∈ [w,n+w) Vj ∈ [n,n+w) right[] <- x[i][j]; // Send right
14     Vi ∈ [n,n+w) Vj ∈ [w,n+w) up[] <- x[i][j]; // Send left
15     Vi ∈ [w,n+w) Vj ∈ [0,w) x[i][j] <- left[]; // Receive from left
16     Vi ∈ [0,w) Vj ∈ [w,n+w) x[i][j] <- down[]; // Receive from below
17   }
18   parallel {
19     Vi ∈ [n,n+w) Vj ∈ [0,w) up[] <- x[i][j]; // Send corner data received from left to above
20     Vi ∈ [0,w) Vj ∈ [0,w) x[i][j] <- down[]; // Receive corner data from below
21   }
22 }
23
24 function compute() {
25   let i ∈ [0,n);
26   let j ∈ [0,n);
27   sp a;
28   a = avec[0];
29   Vi Vj y[i+w][j+w] = a*x[i+p ][j+p-1];
30   a = avec[1];
31   Vi Vj y[i+w][j+w] += a*x[i+p-1][j+p ];
32   a = avec[2];
33   Vi Vj y[i+w][j+w] += a*x[i+p+1][j+p ];
34   a = avec[3];
35   Vi Vj y[i+w][j+w] += a*x[i+p ][j+p+1];
36   a = avec[4];
37   Vi Vj y[i+w][j+w] += a*x[i+p ][j+p ];
38
39   Vi Vj x[i+w][j+w] = y[i+w][j+w];
40 }
41
42 function innerloop(sp niter) {
43   sp iter = 0.0;
44
45   while(iter < niter) {
46     sendrecv();
47     compute();
48     iter += 1.0;
49   }
50 }

```

Table 3. Main time-stepping loop for the 5-point stencil heat equation code, including complete communication and computation functions. The *parallel* clause expresses all statements in the block may in parallel. This allows concurrent communication in different directions and is supported by hardware micro-threads. The \forall -statements is a compact loop notation, which the compiler uses to infer generation of vector-instructions.

3.2 Numerical Methods

3.2.1 Heat Equation. Five-point stencils can numerically solve second order PDEs of the form $\dot{u} = Au_{xx} + Cu_{yy} + Du_x + Eu_y$. A linear combination of each point's neighbors provide local approximations for the directional derivatives. Adding one to the central coefficient and scaling all terms by a finite Δt implements Eulerian time integration via recursively replacing its input. We implemented and thoroughly characterized a generic five-point stencil with fixed coefficients.

| System | Field Vars | FLOPs |
|----------------------|------------|-------|
| HE, 5-point stencil | 1 | 9 |
| HE, 9-point stencil | 1 | 17 |
| SWE (even half-step) | 3 | 94 |
| SWE (odd half-step) | 4 | 61 |
| SWE (full time-step) | 7 | 155 |

Table 4. Hyperparameters of analyzed workloads

The heat equation is a familiar example that fits this form. Each iteration therefore performs five multiplications and four additions for a total nine FLOPs per point per step (Table 4). The 9-point stencil is similar, except it uses 8 immediate neighbors of each grid point in the computation, and performs 17 FLOPs per grid point per time-step.

3.2.2 Shallow Water Equations. The shallow water equations (SWE) define a system of non-linear hyperbolic conservation laws. These are PDEs that model inviscid fluid flow for systems where length scale is much greater than the depth scale. They result from depth integration of the incompressible Navier-Stokes equations. SWE models velocity and fluid height subject to gravity, Coriolis force, and oceanic topography. Our simulation uses the Mercator projection so that the grid has a flat topology. In the resulting latitude-longitude coordinates, SWE takes the form

$$\begin{aligned}\frac{\partial u}{\partial t} + \mathbf{v} \cdot \nabla u - \left(\ell + \frac{u}{a} \tan \phi \right) v + \frac{g}{a \cos \phi} \frac{\partial h}{\partial \lambda} &= 0, \\ \frac{\partial v}{\partial t} + \mathbf{v} \cdot \nabla v + \left(\ell + \frac{u}{a} \tan \phi \right) u + \frac{g}{a} \frac{\partial h}{\partial \phi} &= 0, \\ \frac{\partial s}{\partial t} + \mathbf{v} \cdot \nabla s + \frac{s}{a \cos \phi} \left(\frac{\partial u}{\partial \lambda} + \frac{\partial [v \cos \phi]}{\partial \phi} \right) &= 0,\end{aligned}$$

where g is the gravitational acceleration, a is the Earth's radius, ℓ is the Coriolis coefficient, λ is the longitude, ϕ is the latitude, and $\mathbf{v} = (u, v)$.

The SWE field variables are surface velocity (u, v) and water surface height h . The method uses a constant field for oceanic topography b defined as the distance from Earth's center and represented relative to a reference sphere with radius just below the lowest abysmal point to avoid loss of precision. The variable s denotes the water depth, $s = h - b$. Additionally, we maintain constant fields: a shoreline indicator field encodes the water boundary to enforce a no-slip condition; pre-computed sine, cosine, and secants (of latitude) allow the method to work in latitude-longitude coordinates.

We use a Lax-Wendroff spatial discretization and a two-stage Runge-Kutta (RK2) time integration scheme. This uses *cell center* half steps in space and time to achieve a second-order estimate of field evolution. The second-order method provides conservation, higher accuracy over longer intervals and stability for hyperbolic PDEs. This permits taking larger time steps. Indeed, solving hyperbolic problems requires a time integrator that includes an interval of the imaginary axis as part of its stability region in the plane of complex numbers. This disqualifies Eulerian time-stepping approaches.

The first half step has 94 FLOPs and computes 4 neighborhood fields. The second half step has 61 FLOPs and computes 3 neighborhood fields. In total, each full time-step has 155 FLOPs, computing 7 neighborhood fields, and remaps the grid twice.

3.3 The Wafer-Scale Engine Cluster

A wafer-scale engine (WSE) [23] is a system built with the largest processor chip ever produced, and is an example of a spatial architecture. A WSE comprises a 2D grid of tiles, each composed of a processing element (PE), local memory, and a router. Each router has five ports, connecting one each to its immediate cardinal neighbors and to the local PE. Routers forward 32-bit messages called *wavelets* with very low, order nanosecond latency. Each router has 24 virtual channels. A virtual channel multicasts traffic arriving from any one of the five ports to any subset of the five ports. Routers can be dynamically reconfigured in response to specially formatted wavelets.

Specialized tiles designated for off-wafer IO live along the left and right edges of the wafer. In total, there are 132 IO tiles, with 66 per side on the left and right.

We used a cluster of 64 WSE nodes for our experiments. In the cluster, the i^{th} wafer's j^{th} port connects to the j^{th} switch's i^{th} port (Figure 4). Each node has twelve 100 Gbps ports, thus with a collection of twelve 64-port switches, the wafers are fully interconnected.

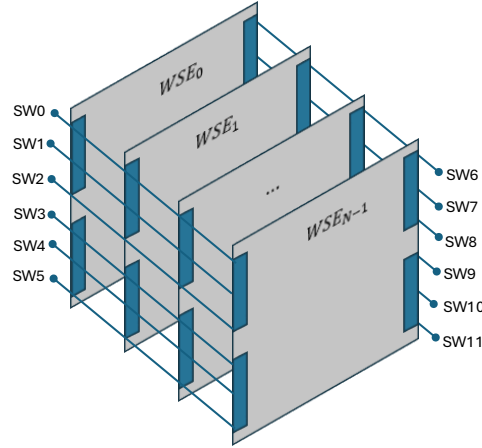


Fig. 4. Switch Topology for an arbitrary number of WSEs. The same port index for all wafers in a cluster live on the same network switch.

Wafer communication ports are on the right and left fabric edges. The program's core array receives data from its left and bottom edges and transmits toward the top and right. Accordingly, the horizontally directed traffic receives from the wafer's left edge and sends to the right. The vertically directed traffic routes with a 90-degree turn send to the left edge and receive from the right edge (Figure 6).

The node-to-node network links including the order 2,000 tile network hops and ethernet switch to bridge vertically adjacent subdomains has a routing latency of about $10\mu\text{s}$. The average link latency for using the sequential node performance model (Section 4.1) is about $1000^{-1}(10\mu\text{s} + 1000\text{ns}) = 1.1\text{ns}$. The domain translation algorithm allows us to benefit from the low average link latency whereas ghost methods are limited by the worst-case $10\mu\text{s}$ latency.

The physical wafer interconnection does not match the desired application interconnection: physically, every wafer's right-hand side is connected, whereas the application needs to send from the rightmost extent of its grid to the leftmost extent of an adjacent node's grid. To handle this we compile the program as two mirror-image variants. The nodes are

| Parameter | Dimension | Values | Parameter Range |
|--------------|---------------|---|----------------------------------|
| Weak Scale | (nodes) | 1, 2^2 , 4^2 , 4×6 , 2×30 , 6×10 , 8^2 | 1 - 64 wafer-scale nodes |
| Strong Scale | (points/core) | 2^2 , 4^2 , 8^2 , 16^2 , 32^2 , 64^2 | 4 - 4k grid points per core |
| Node Size | (core/node) | 720^2 , 744×1116 | 500k and 900k cores per node |
| Node Clock | (GHz) | 0.75, 1.2 | 0.8 - 2 PFLOP/s peak performance |

Table 5. Parameters settings used in grid sweep for performance characterization.

assigned variants in a checkerboard pattern (Figure 5). The checkerboard pattern constrains cluster to having multiples of four nodes.

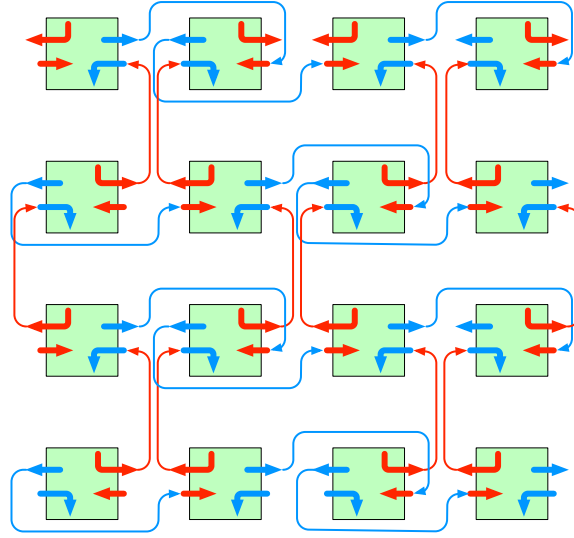


Fig. 5. An example cluster topology showing the original spatial stencil and its Y-axis mirror which alternate between every wafer in the cluster. Mirroring enables data to enter and exit through the same switch, minimizing communication latency.

4 Performance Characterization

This section describes the specific experiments we ran for the close match between the overfed and predicted performance for the implementation.

4.1 Methodology

To assess scaling and fit a performance model, we ran a sweep of performance tests varying weak scale, strong scale, and node performance (Table 5). At regular timestep intervals, all cores record their 48-bit hardware clock-cycle counter to local memory. Instrumented runs produce an array with dimensions $(\text{cluster}_w \times \text{cluster}_h \times \text{ncore}_w \times \text{ncore}_h \times \text{samples})$. For large runs (50M cores, 1000 samples) this produces 300 GB of telemetry. Therefore we only retain data from a subset of cores for analysis.

We fit measurements to a performance model. The model uses the minimum of compute-bound performance and IO-bound performance. Because the domain translation algorithm renders latency irrelevant, we do not include it in the model.

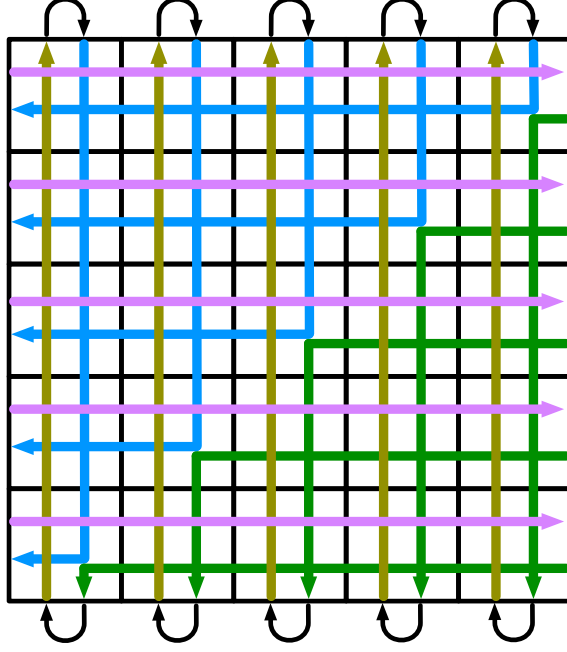


Fig. 6. On-wafer routing. Horizontal flow (purple) enters the node’s left edge and creates a daisy chain between every pair of horizontally adjacent cores. It egresses the system’s right edge. Vertical flow (dark green) enters from the right edge and makes a turn toward the bottom edge. The bottom row of cores receive this message and retransmit it upwards in a daisy chain (light green) among every pair of vertically adjacent cores. The top row of cores transmit the message back down (blue) with a turn to egress the node at its left edge. This scheme uses 8 virtual channels. Both daisy chains use two virtual channels alternating channels on an even/odd scheme. Both turns use two virtual channels with the change occurring at the bend.

| Code | Performance model | Flops/step | Asymptotic utilization |
|---------------|-----------------------------------|------------|------------------------|
| 5-pt heat eq. | $f(n) = 105 + 3.74n + 6.72n^2$ | $9n^2$ | 67% |
| 9-pt heat eq. | $f(n) = 97 + 3.5n + 9.37n^2$ | $17n^2$ | 91% |
| SWE | $f(n) = 1026 + 183.2n + 137.6n^2$ | $155n^2$ | 56% |

Table 6. Performance models for different PDE simulations. The models were fit to single node experiments not using external I/O. $f(n)$ gives the estimated cost of one timestep in clock cycles. n indicate the problem size, where the number of grid points per core is $n \times n$. The utilization is measured in fraction of peak flops/s (2/cycle)

We fit models to three different codes: the heat equation with 5- and 9-point stencils, and the Shallow Water equations. The compute cost of the performance models are shown in Table 6. In the limit of large n , all model become compute bound, and the asymptotic utilization is shown in the table.

We characterize a node’s compute-bound performance in an IO-unconstrained environment. Here, on-wafer routing directly bridges opposite edges of the core array. We regress iteration time’s dependence on grid points per core as $t = \sum_{i=0}^d a_i n^i$.

IO-bound performance is assessed by measuring link payload per iteration. We independently regress horizontal and vertical payloads as $(b_0, b_1, b_2) \cdot (nw_w, w_w, 1)$ and $(d_0, d_1, d_2) \cdot (nw_h, w_h, 1)$. The current implementation has two IO limitations:

- (1) In their vertical transmissions each core sends its horizontal neighbor points. At the node-to-node level this is redundant. A periodic data filter on node transmit coupled with data replication upon receive would achieve $b_1 = 0$. This is significant for our implementation because we have large w and small n .
- (2) We provision dedicated vertical and horizontal communication channels each with the same total number of IO links. This means that the maximum of horizontal and vertical payloads limits performance. With optimization the average (not the max) will limit performance.

4.2 Measured results

Using the heat equation as our baseline experiment, we conducted a range of experiments on a cluster of wafer-scale CS-3 systems [32]. We varied the number of nodes and the number of grid points per core (Table 5). We used the resulting measurements to assess the weak scaling of the performance measured in time steps per second. While varying the number of CS-3 nodes from 4 to 64, we observed near-perfect weak scaling with a remarkably consistent performance for each setting of grid point number per core (Figure 7).

The observed performance was very consistent between runs with extremely low relative variances of measurements with different node counts. We observed weak scaling efficiencies ranging from 98.8% ($n = 2$) to 99.9998% ($n = 64$) when scaling from 4 to 60 nodes. It is reasonable to ask whether the experimental setup has the fidelity to report a result to six significant figures. The measurement is a hardware clock cycle counter (accurate to the nanosecond) for a period of 255,000 time steps with each contributing over 1,000 cycles. Therefore, the raw data has fidelity to 9 figures.

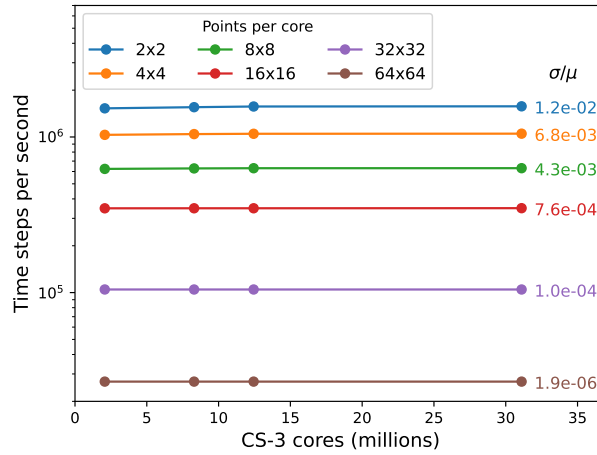


Fig. 7. Weak scaling of the heat equation for runs on 4 to 60 CS-3 node counts. The observed performance was remarkably consistent for each points/core setting.

For all experiments that we conducted, the number of grid points on each CS-3 system was sufficient to fully hide the cross-node communication latency, but the specific choice resulted in either compute-bound or IO bandwidth-bound behavior. We applied the model described in Section 4.1 and compared model predictions to the measured data. Figure 8 shows this comparison expressed as FLOP/core/s. We can see that using fewer than 256 points per core results in communication-bound behavior. As we use more points per core, the computation cost grows faster than that of the

communication and the computation reaches its compute bound. In the compute-bound regime we observe up to 1.32 flops per cycle, which is 66% of the single precision peak of 2 flops per cycle on the CS-3 system.

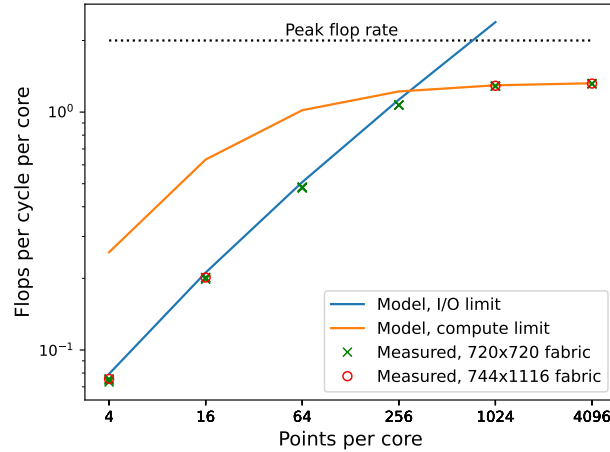


Fig. 8. Comparison of model prediction with measured results. The model correctly shows the cross-over between IO-bound and compute-bound behavior.

Having established a strong alignment of model predictions with measured data, we can plot strong scaling. The left panel of Figure 9 shows our performance model, including I/O, for scaling problems of various sizes across 4 to 128 CS-3 nodes, as well as data points measured on cluster simulations. We see close agreement between our model and real measured performance. Our systems allow boosting the clock frequency from the standard 750MHz up to 1.2GHz. At this operating point, the system is power constrained and can throttle significantly. We created a power optimized version of the 9-point heat equation that takes advantage of a small cache of power efficient memory in each core. The right panel of Figure 9 weak scaling performance for this code operating at 1.2GHz with 3 billion grid points per node. The weak scaling behavior is nearly perfect and we achieved 84.7 PFLOPS using 64 nodes. We plan to extend our work to larger clusters and expect to observe increased performance consistent with model predictions.

The power specification per CS-3 node is 23kW. Thus, the power-efficient performance of the 64-node CS-3 cluster measures at 57 GFLOPs per Watt. In comparison, the current leader of Green500 (JEDI) achieves 72.7 GFLOPs per Watt on a dense linear algebra workload [31]. To the best of our knowledge, there is no sparse computation on any cluster that is near the efficiency we observe with the CS-3 cluster.

We tested the domain translation method for shallow water equations using the GEBCO_2024 Grid [13]. The data set offers a global continuous terrain model for ocean and land with a spatial resolution of 15 arc seconds or 462 meters.

Figure 10 shows the outcome of asteroid impact in the ocean. The asteroid disintegrates or ends at the ocean floor. Its kinetic energy dissipates as thermal and mechanical energy in the ocean. We simulate the impact as a sine hump of water elevated above the surface of the ocean whose potential energy equals 90% of the impact kinetic energy (2.4M tons of TNT equivalent). The sine hump is an initial condition given as input to the SWE model, which simulates the resulting waves via numerical solution of PDEs. In this example, the sine hump spans 30K km², elevates to 200 m above

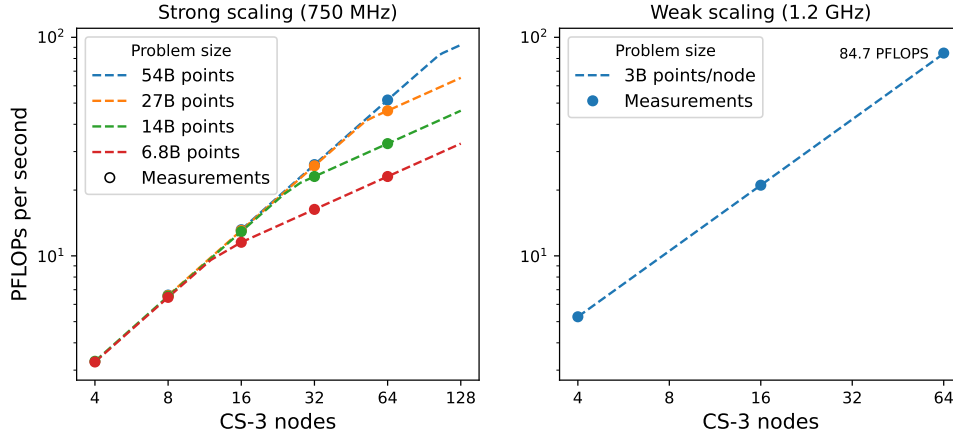


Fig. 9. (left) Strong scaling for the 5-point heat equation code on different number of WSE nodes, configured at the standard 750 MHz clock frequency. It shows perfect scaling up to 64 nodes for the largest simulations, and very close agreement with the performance model. (right) Weak scaling for 9-point heat equation on clock-boosted system. The code was specially optimized to reduce power throttling at the higher clock frequency. On 64 nodes and 192 billion grid points, we achieved 84.7 PFlops.

the ocean surface at its highest, and contains 5.8T m³ of water. This simulates the energy of a 2M kg asteroid impacting at 100 km/s. Figure 11 shows the wave impact zoomed at San Francisco Bay.

As with the heat equation, we observed near-perfect weak scaling across multiple CS-3 nodes. We also measured more than one sustained flop per cycle in the compute-bound regime.

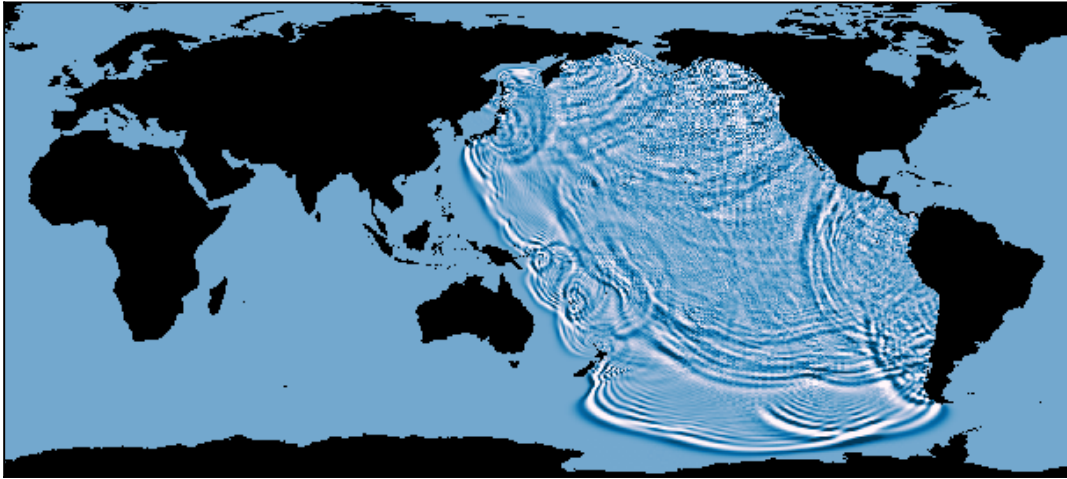


Fig. 10. Planetary-scale tsunami wave propagation 14 hours after asteroid impact with energy of 2.4M tons of TNT equivalent.

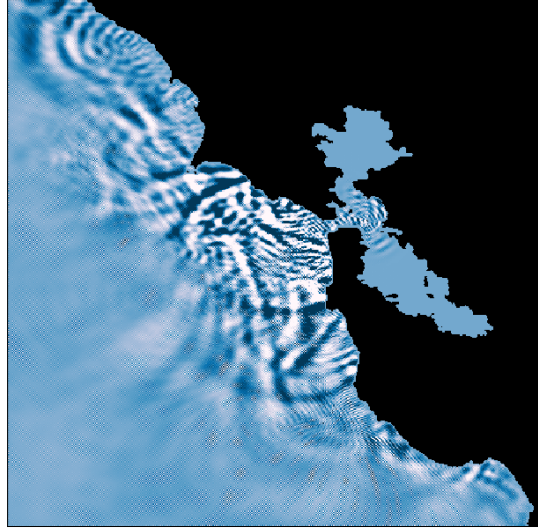


Fig. 11. Wave impact at San Francisco Bay

5 Conclusions

A central implication of this work is a pathway to achieve unprecedented performance for physical system modeling. We demonstrated that we can maintain high system efficiency on a large distributed cluster at a fine-grain parallelism. This delivers scaling not only in the spatial domain (i.e., weak scaling) but also in the time domain (i.e., strong scaling). This enables study of large scale systems in ways that were previously impossible or cost and time prohibitive. This has significant implications for study of long time horizon physics, uncertainty quantification, design optimization, cyberphysical security, and real time digital twinning. We have shown that it is possible to extend our previous research on single-device PDE solutions to multi-device with little to no deterioration in calculation speed.

For these reasons, we were careful to demonstrate a meaningful result for science at planetary scale. The shallow water equations solved here represent the core of several important geophysical applications. In addition to the tsunami application described above, shallow water solvers are critical components of both atmospheric and oceanic modeling. In these disciplines, one first constructs a shallow water model to test numerics and computational implementation, and then extends these models to three-dimensional atmosphere and ocean models used for numerical weather prediction and earth system modeling. For example, the state-of-the-art CESM, E3SM, FV3 and MPAS atmosphere and ocean models ([4, 7, 11, 22, 25, 26] are derived from the shallow water models given in [21, 29, 30]).

The two-dimensional shallow water equations are an ideal first step in the development of these models because they capture the large scale dynamics which dominate the flow and the wave propagation behavior that controls the timestep. To develop a full atmosphere model from a shallow water code, one first adds vertical layers referred to as *stacked shallow water*, followed by vertical coupling between the terms and additional prognostic variables for vertical velocity, temperature and various water species.

Because of the 2D domain decomposition used in modern atmosphere and ocean models, the parallel performance of stacked shallow water equations is an excellent model for the performance of the full equation set. This is because

the nearest neighbor communication patterns will be nearly identical and the ratio of floating point operations to communication will be quite similar. Evolving a stacked shallow water model into a full atmospheric model involves many additional prognostic variables and associated computations, but the extra work is all on-processor, resulting in a slower model but with improved strong scaling. The stacked shallow water system represents the core computational bottleneck in modern numerical weather prediction and earth system modeling.

Our results running shallow water equations on the Cerebras system demonstrate the promise of this architecture for atmosphere and ocean models critical for weather prediction and earth systems assessments. These models traditionally run at less than 5% of peak [3]. Extending our shallow water approach to a full model running at 60% of peak would thus represent a breakthrough in performance per Watt and also in terms of total achievable throughput.

References

- [1] Dennis Abts, Jonathan Ross, Jonathan Sparling, Mark Wong-VanHaren, Max Baker, Tom Hawkins, Andrew Bell, John Thompson, Temesghen Kahsai, Garrin Kimmell, et al. 2020. Think fast: A tensor streaming processor (TSP) for accelerating deep learning workloads. In *2020 ACM/IEEE 47th Annual International Symposium on Computer Architecture (ISCA)*. IEEE, 145–158.
- [2] Francis Alexander, Ann Almgren, John Bell, Amitava Bhattacharjee, Jacqueline Chen, Phil Colella, David Daniel, Jack DeSlippe, Lori Diachin, Erik Draeger, et al. 2020. Exascale applications: skin in the game. *Philosophical Transactions of the Royal Society A* 378, 2166 (2020), 20190056.
- [3] Jessie C. Carman, Thomas Clune, Francis Giraldo, Mark Govett, Anke Kamrath, Tsengdar Lee, David McCarren, John Michalakes, Scott Sandgathe, and Tim Whitcomb. 2017. Position paper on high performance computing needs in Earth system prediction. (2017). <https://doi.org/10.7289/V5862DH3>
- [4] Johann Dahm, Eddie Davis, Florian Deconinck, Oliver Elbert, Rhea George, Jeremy McGibbon, Tobias Wicky, Elynn Wu, Christopher Kung, Tal Ben-Nun, Lucas Harris, Linus Groner, and Oliver Fuhrer. 2023. Pace v0.2: a Python-based performance-portable atmospheric model. *Geoscientific Model Development* 16, 9 (May 2023), 2719–2736. <https://doi.org/10.5194/gmd-16-2719-2023>
- [5] James Demmel, Mark Hoemmen, Marghoob Mohiyuddin, and Katherine A. Yelick. 2008. Avoiding communication in sparse matrix computations. In *22nd IEEE International Symposium on Parallel and Distributed Processing, IPDPS 2008, Miami, Florida USA, April 14-18, 2008*. IEEE, 1–12. <https://doi.org/10.1109/IPDPS.2008.4536305>
- [6] Chris H. Q. Ding and Yun He. 2001. A ghost cell expansion method for reducing communications in solving PDE problems. In *Proceedings of the 2001 ACM/IEEE conference on Supercomputing, Denver, CO, USA, November 10-16, 2001, CD-ROM*, Greg Johnson (Ed.). ACM, 50. <https://doi.org/10.1145/582034.582084>
- [7] A. S. Donahue, P. M. Caldwell, L. Bertagna, H. Beydoun, P. A. Bogenschutz, A. M. Bradley, T. C. Clevenger, J. Foucar, C. Golaz, O. Guba, W. Hannah, B. R. Hillman, J. N. Johnson, N. Keen, W. Lin, B. Singh, S. Sreepathi, M. A. Taylor, J. Tian, C. R. Terai, P. A. Ullrich, X. Yuan, and Y. Zhang. 2024. To Exascale and Beyond—The Simple Cloud-Resolving E3SM Atmosphere Model (SCREAM), a Performance Portable Global Atmosphere Model for Cloud-Resolving Scales. *Journal of Advances in Modeling Earth Systems* 16, 7 (2024). <https://doi.org/10.1029/2024ms004314>
- [8] EESA. 2025. Close Approaches. <https://neo.ssa.esa.int/close-approaches>.
- [9] Haohuan Fu, Lin Gan, Chao Yang, Wei Xue, Lanning Wang, Xinliang Wang, Xiaomeng Huang, and Guangwen Yang. 2017. Solving global shallow water equations on heterogeneous supercomputers. *PLoS one* 12, 3 (2017), e0172583.
- [10] Haohuan Fu, Junfeng Liao, Nan Ding, Xiaohui Duan, Lin Gan, Yishuang Liang, Xinliang Wang, Jinzhe Yang, Yan Zheng, Weiguo Liu, Lanning Wang, and Guangwen Yang. 2017. Redesigning CAM-SE for peta-scale climate modeling performance and ultra-high resolution on Sunway TaihuLight. In *Proceedings of the International Conference for High Performance Computing, Networking, Storage and Analysis (Denver, Colorado) (SC '17)*. Association for Computing Machinery, New York, NY, USA, Article 1, 12 pages. <https://doi.org/10.1145/3126908.3126909>
- [11] Jean-Christophe Golaz, Luke P. Van Roekel, Xue Zheng, Andrew F. Roberts, Jonathan D. Wolfe, Wuyin Lin, Andrew M. Bradley, Qi Tang, Mathew E. Maltrud, Ryan M. Forsyth, Chengzhu Zhang, Tian Zhou, Kai Zhang, Charles S. Zender, Mingxuan Wu, Hailong Wang, Adrian K. Turner, Balwinder Singh, Jadwiga H. Richter, Yi Qin, Mark R. Petersen, Azamat Mametjanov, Po-Lun Ma, Vincent E. Larson, Jayesh Krishna, Noel D. Keen, Nicole Jeffery, Elizabeth C. Hunke, Walter M. Hannah, Oksana Guba, Brian M. Griffin, Yan Feng, Darren Engwirda, Alan V. Di Vittorio, Cheng Dang, LeAnn M. Conlon, Chih-Chieh-Jack Chen, Michael A. Brunke, Gautam Bisht, James J. Benedict, Xylar S. Asay-Davis, Yuying Zhang, Meng Zhang, Xubin Zeng, Shaocheng Xie, Phillip J. Wolfram, Tom Vo, Milena Veneziani, Teklu K. Tesfa, Sarat Sreepathi, Andrew G. Salinger, J. E. Jack Reeves Eyre, Michael J. Prather, Salil Mahajan, Qing Li, Philip W. Jones, Robert L. Jacob, Gunther W. Huebler, Xianglei Huang, Benjamin R. Hillman, Bryce E. Harrop, James G. Foucar, Yilin Fang, Darin S. Comeau, Peter M. Caldwell, Tony Bartoletti, Karthik Balaguru, Mark A. Taylor, Renata B. McCoy, L. Ruby Leung, and David C. Bader. 2022. The DOE E3SM Model Version 2: Overview of the Physical Model and Initial Model Evaluation. *Journal of Advances in Modeling Earth Systems* 14, 12 (2022), e2022MS003156. <https://doi.org/10.1029/2022MS003156>
- [12] Mark Govett, Bubacar Bah, Peter Bauer, Dominique Berod, Veronique Bouchet, Susanna Corti, Chris Davis, Yihong Duan, Tim Graham, Yuki Honda, Adrian Hines, Michel Jean, Junishi Ishida, Bryan Lawrence, Jian Li, Juerg Luterbacher, Chiasi Muroi, Kris Rowe, Martin Schultz, Martin Visbeck, and Keith Williams. 2024. Exascale Computing and Data Handling: Challenges and Opportunities for Weather and Climate Prediction. *Bulletin of the American Meteorological Society* 105, 12 (2024), E2385 – E2404. <https://doi.org/10.1175/BAMS-D-23-0220.1>

- [13] GEBCO Compilation Group. 2024. GEBCO 2024 Grid [data set]. <https://doi.org/10.5285/1c44ce99-0a0d-5f4f-e063-7086abc0ea0f> Accessed: 2025-03-28.
- [14] Mark Hoemmen. 2010. *Communication-avoiding Krylov subspace methods*. Ph.D. Dissertation. University of California, Berkeley, USA. <http://www.escholarship.org/uc/item/7757521k>
- [15] JPL. 2025. Asteroid Watch. <https://www.jpl.nasa.gov/asteroid-watch/next-five-approaches/>.
- [16] Fredrik Berg Kjolstad and Marc Snir. 2010. Ghost Cell Pattern. In *Proceedings of the 2010 Workshop on Parallel Programming Patterns* (Carefree, Arizona, USA) (*ParaPLoP '10*). Association for Computing Machinery, New York, NY, USA, Article 4, 9 pages. <https://doi.org/10.1145/1953611.1953615>
- [17] Douglas Kothe, Stephen Lee, and Irene Qualters. 2019. Exascale Computing in the United States. *Computing in Science & Engineering* 21, 1 (2019), 17–29. <https://doi.org/10.1109/MCSE.2018.2875366>
- [18] Sean Lie. 2023. Cerebras Architecture Deep Dive: First Look Inside the Hardware/Software Co-Design for Deep Learning. *IEEE Micro* 43, 3 (2023), 18–30.
- [19] Andreas Müller, Michal A Kopera, Simone Marras, Lucas C Wilcox, Tobin Isaac, and Francis X Giraldo. 2019. Strong scaling for numerical weather prediction at petascale with the atmospheric model NUMA. *The International Journal of High Performance Computing Applications* 33, 2 (2019), 411–426.
- [20] Raghu Prabhakar, Yaqi Zhang, David Koeplinger, Matt Feldman, Tian Zhao, Stefan Hadjis, Ardavan Pedram, Christos Kozyrakis, and Kunle Olukotun. 2017. Plasticine: A reconfigurable architecture for parallel patterns. *ACM SIGARCH Computer Architecture News* 45, 2 (2017), 389–402.
- [21] William M. Putman and Shian-Jiann Lin. 2007. Finite-volume transport on various cubed-sphere grids. *J. Comput. Phys.* 227, 1 (Nov. 2007), 55–78. <https://doi.org/10.1016/j.jcp.2007.07.022>
- [22] Todd Ringler, Mark Petersen, Robert L. Higdon, Doug Jacobsen, Philip W. Jones, and Mathew Maltrud. 2013. A multi-resolution approach to global ocean modeling. *Ocean Modelling* 69 (Sept. 2013), 211–232. <https://doi.org/10.1016/j.ocemod.2013.04.010>
- [23] Kamil Rocki, Dirk Van Essendelft, Ilya Sharapov, Robert Schreiber, Michael Morrison, Vladimir Kibardin, Andrey Portnoy, Jean-Francois Dietiker, Madhava Syamlal, and Michael James. 2020. Fast stencil-code computation on a wafer-scale processor. In *Proceedings of the International Conference for High Performance Computing, Networking, Storage and Analysis, SC 2020, Virtual Event / Atlanta, Georgia, USA, November 9-19, 2020*, Christine Cuicchi, Irene Qualters, and William T. Kramer (Eds.). IEEE/ACM, 58.
- [24] Kylee Santos, Stan Moore, Tomas Oppelstrup, Amirali Sharifian, Ilya Sharapov, Aidan Thompson, Delyan Z. Kalchev, Danny Perez, Robert Schreiber, Scott Pakin, Edgar A. Leon, James H. Laros, Michael James, and Sivasankaran Rajamanickam. 2024. Breaking the Molecular Dynamics Timescale Barrier Using a Wafer-Scale System. In *Proceedings of the International Conference for High Performance Computing, Networking, Storage and Analysis* (Atlanta, GA, USA) (*SC '24*). ACM, New York, NY, USA. <https://doi.org/10.1109/SC41406.2024.00014>
- [25] William C. Skamarock, Joseph B. Klemp, Michael G. Duda, Laura D. Fowler, Sang-Hun Park, and Todd D. Ringler. 2012. A Multiscale Nonhydrostatic Atmospheric Model Using Centroidal Voronoi Tessellations and C-Grid Staggering. *Monthly Weather Review* 140, 9 (Sept. 2012), 3090–3105. <https://doi.org/10.1175/mwr-d-11-00215.1>
- [26] R. Justin Small, Julio Bacmeister, David Bailey, Allison Baker, Stuart Bishop, Frank Bryan, Julie Caron, John Dennis, Peter Gent, Hsiao-ming Hsu, Markus Jochum, David Lawrence, Ernesto Muñoz, Pedro diNezio, Tim Scheitlin, Robert Tomas, Joseph Tribbia, Yu-heng Tseng, and Mariana Vertenstein. 2014. A new synoptic scale resolving global climate simulation using the Community Earth System Model. *Journal of Advances in Modeling Earth Systems* 6, 4 (Dec. 2014), 1065–1094. <https://doi.org/10.1002/2014ms000363>
- [27] Barry F. Smith, Petter E. Bjørstad, and William D. Gropp. 1996. *Domain decomposition: parallel multilevel methods for elliptic partial differential equations*. Cambridge University Press, USA.
- [28] Emil Talpes, Debjit Das Sarma, Doug Williams, Sahil Arora, Thomas Kunjan, Benjamin Floering, Ankit Jalote, Christopher Hsiong, Chandrasekhar Poorna, Vaidehi Samant, John Sicilia, Anantha Kumar Nivarti, Raghuvir Ramachandran, Tim Fischer, Ben Herzberg, Bill McGee, Ganesh Venkataramanan, and Pete Banon. 2023. The Microarchitecture of DOJO, Tesla's Exa-Scale Computer. *IEEE Micro* 43, 3 (2023), 31–39. <https://doi.org/10.1109/MM.2023.3258906>
- [29] M. A. Taylor and A. Fournier. 2010. A compatible and conservative spectral element method on unstructured grids. *J. Comput. Phys.* 229 (2010), 5879–5895. <https://doi.org/10.1016/j.jcp.2010.04.008>
- [30] John Thuburn, Todd D Ringler, William C Skamarock, and Joseph B Klemp. 2009. Numerical representation of geostrophic modes on arbitrarily structured C-grids. *J. Comput. Phys.* 228, 22 (2009), 8321–8335.
- [31] Top500. 2024. Green500. <https://top500.org/lists/green500/2024/11/>.
- [32] James Wang. 2024. Cerebras CS-3: the world's fastest and most scalable AI accelerator - Cerebras. <https://www.cerebras.ai/blog/cerebras-cs3>. Accessed: 2025-03-20.
- [33] Samuel Williams, Andrew Waterman, and David Patterson. 2009. Roofline: an insightful visual performance model for multicore architectures. *Commun. ACM* 52, 4 (April 2009), 65–76. <https://doi.org/10.1145/1498765.1498785>
- [34] Mino Woo, Terry Jordan, Robert Schreiber, Ilya Sharapov, Shaheer Muhammad, Abhishek Koneru, Michael James, and Dirk Van Essendelft. 2022. Disruptive Changes in Field Equation Modeling: A Simple Interface for Wafer Scale Engines. *CoRR* abs/2209.13768 (2022). arXiv:2209.13768
- [35] Chao Yang, Wei Xue, Haohuan Fu, Hongtao You, Xinliang Wang, Yulong Ao, Fangfang Liu, Lin Gan, Ping Xu, Lanning Wang, et al. 2016. 10M-core scalable fully-implicit solver for nonhydrostatic atmospheric dynamics. In *SC'16: Proceedings of the International Conference for High Performance Computing, Networking, Storage and Analysis*. IEEE, 57–68.

- [36] Y. Ye, Z. Song, S. Zhou, Y. Liu, Q. Shu, B. Wang, W. Liu, F. Qiao, and L. Wang. 2022. swNEMO_v4.0: an ocean model based on NEMO4 for the new-generation Sunway supercomputer. *Geoscientific Model Development* 15, 14 (2022), 5739–5756. <https://doi.org/10.5194/gmd-15-5739-2022>